A novel biomechanical model of the mouse forelimb predicts muscle activity in optimal control simulations of reaching movements

Jesse I. Gilmer[1], Susan K. Coltman[5], Geraldine Cuenu[2], John R. Hutchinson[4], Daniel Huber[2], Abigail L. Person[3], and Mazen Al Borno[1]

1. University of Colorado Denver | Anschutz Medical Campus, Department of Computer Science and Engineering, Computational Bioscience Program
2. University of Geneva, Department of Basic Neuroscience
3. University of Colorado Denver | Anschutz Medical Campus, Department of Physiology and Biophysics
4. Royal Veterinary College, Department of Comparative Biomedical Sciences
5. The Pennsylvania State University, Department of Kinesiology

ABSTRACT

Mice are key model organisms in neuroscience and motor systems physiology. Fine motor control tasks performed by mice have become widely used in assaying neural and biophysical motor system mechanisms. Although fine motor tasks provide useful insights into behaviors which require complex multi-joint motor control, there is no previously developed physiological biomechanical model of the adult mouse forelimb available for estimating kinematics nor muscle activity or kinetics during behaviors. Here, we developed a musculoskeletal model based on high-resolution imaging of the mouse forelimb that includes muscles spanning the neck, trunk, shoulder, and limbs. Physics-based optimal control simulations of the forelimb model were used to estimate *in vivo* muscle activity present when constrained to the tracked kinematics during reaching movements. The activity of a subset of muscles was recorded and used to assess the accuracy of the muscle patterning in simulation. We found that the synthesized muscle patterning in the forelimb model had a strong resemblance to empirical muscle patterning, suggesting that our model has utility in providing a realistic set of estimated muscle excitations over time when given a kinematic template. The strength of the similarity between empirical muscle activity and optimal control predictions increases as mice performance improves throughout learning of the reaching task. Our computational tools are available as open-source in the OpenSim physics and modeling platform. Our model can enhance research into limb control across broad research topics and can inform analyses of motor learning, muscle synergies, neural patterning, and behavioral research that would otherwise be inaccessible.

NEW & NOTEWORTHY

Investigations into motor planning and execution lack an accurate and complete model of the forelimb, which could bolster or expand on findings. We sought to construct such a model using high detail scans of murine anatomy and prior research into muscle physiology. We then used the model to predict muscle excitations in a set of reaching movements and found that it provided accurate estimations and provided insight into an optimal-control framework of motor learning.

Motor control; biophysical models; reaching behaviors; muscle patterning; optimal control

INTRODUCTION

Mus musculus (Mice) are key model organisms for behavioral studies in neuroscience and physiology, including for tasks that assay fine motor control and motor learning. Mice can perform tasks such as manipulandum control (Bollu et al., 2019), dexterous reach (Becker et al., 2020, Fleischer et al., 2023; Khanna et al., 2021; Yang et al., Wagner et al., 2021), and can learn complex behaviors with and without training (Burgess et al. 2017, Serradj et al., 2023, Sauerbrei et al., 2020, Galinanes et al., 2018, Conner at al., 2021). Mice are a useful organism for studying human disease, and their behaviors reflect an evolutionarily preserved trait applicable to human motor disorders (Iwaniuk 2000). They also convey a benefit to researchers because of their accessible genetics and a slate of powerful molecular tools, which can allow researchers to perturb neural behavior through optogenetics (Deisseroth et al., 2006).

However, despite the utility of mice as a model organism in motor learning, there are no high-resolution reconstructions of the adult mouse forelimb, nor are there any physiological biomechanical models of the mouse forelimb that incorporate fully developed muscle morphology. Biomechanical models are useful tools for motor systems and neuromechanics researchers that can provide detailed insights into muscle activity and limb kinematics (e.g., fiber length and velocities) that would otherwise be difficult or impossible to access through empirical observations. State-of-the-art recording methods can only measure the activity of 3-4 muscles of the 25+ muscles in the murine forelimb (Zia et al., 2020; Chung et al., 2023). Therefore, we set out to construct and evaluate a model of the mouse forelimb, which would be a valuable tool for researchers studying dexterous behaviors in mice.

The only currently available mouse forelimb model, developed recently in a full-body mouse model (Ramalingasetty et al., 2021), was based on mouse embryo data (Delaurier et al., 2008), and lacks many of the large muscles originating from the scapula. Ramalingasetty and colleagues reported that modeling the mouse forelimb was challenging and identified improving their forelimb model as a remaining challenge for future work. Moreover, reference books on limb anatomy present two-dimensional (2D) illustrations of the limb musculature (Hebel 1986), which makes it challenging to extract accurate locations of the attachment points and the three-dimensional (3D) tissue paths from these references (Delaurier et al., 2008). Attachment points have been shown to be the most important factor in estimating how effective a muscle is in producing a joint rotation or moment (Charles et al., 2016). Computing these quantities directly from dissections is challenging because of the size of the forelimb muscles, whose tendon insertion points are separated by as little as tens of microns.

We were able to more accurately identify the muscle attachment sites and muscle paths than previously possible using mouse and rat atlas data through the use of light sheet microscopy. Building on the detailed description of muscle anatomy integrated into a hindlimb biomechanical model by Charles et al. (2016), we aimed to extend this work by developing a similar model for the forelimb using imaging data. We started by scanning and recreating the forelimbs of two adult mice. Muscles with insertions onto the humerus originate from sites that span most of the mouse's trunk and spine, necessitating imaging of much of the mouse body. We limited our reconstruction to muscles that had insertions onto the humerus, radius, and ulna, as reconstruction of muscles with insertions onto the scapula and those that inserted onto the hand was infeasible given the resolution of imaging performed. Once the muscles had been traced and reconstructed, they were used to construct the musculoskeletal geometry of the biomechanical model, including attachments and lines of action, using the OpenSim modeling and physics simulation environment (Delp et al., 2007; Kewley et al., 2024). We used published results on mouse forelimb muscle architecture to

set the muscle parameters (Mathewson et al., 2012). With a model based on highly accurate reconstructions and mouse physiology, we then hypothesized that our model would be well suited to the prediction of muscle activity during motor behaviors such as skilled reaching.

To evaluate the utility of the model, we then aimed to replicate physiological kinematics and predict simultaneously recorded muscle activity. We analyzed a subset of a dataset comprising thousands of reaches from three mice, which included both 3D kinematics and the activity of a subset of muscles involved in the reaching movements (biceps, triceps long head and triceps lateral head electromyography (EMG)). The empirical kinematics were used as constraints when producing muscle-driven synthesized kinematics with optimal control in OpenSim. The empirical EMG was then used as a ground truth for comparison against the optimal control EMG predictions produced in simulation.

We found that optimal control-based simulations using the model were able to recreate reach kinematics accurately using synthesized muscle excitations. When examined against empirical EMG, synthetic EMG closely resembled the mean activation during kinematically matched reaches. These results suggest that our model is capable of replicating realistic reach kinematics and muscle activity. Additionally, we had access to behavioral data that spanned the extent of learning, thus we performed analyses that reveal that the optimal control solutions are closer to the empirical solutions (i.e., the patterns employed by real mice) as reaching performance improves throughout learning. In other words, mice may employ muscle patterning solutions that more closely resemble optimal control solutions as they become more skilled at the task.

More broadly, this model should provide insight into forelimb behaviors that would otherwise be inaccessible by experimental means, and we hope that access to a robust description of the forelimb's kinematics, forces, and muscle activity will advance understanding of mouse behavior. Our computational tools are available as open-source for researchers interested in analyzing muscle activity during mouse forelimb movements.

METHODS

Animals

All procedures followed National Institutes of Health Guidelines and were approved by the Institutional Animal Care and Use Committee at the University of Colorado Anschutz Medical Campus under protocol #43. Animals were housed in an environmentally controlled room, kept on a 12-h light– dark cycle and had ad libitum access to food and water, except during behavioral training and testing as described below. Adult C57BL/6 (Charles River Laboratories) mice of either sex (3 females and 1 male) were used in behavioral experiments. The animals for the light sheet imaging were part of experiments approved by the Animal Care Committee of the University of Geneva and by the veterinary office of the "Direction générale de la santé" of the Canton of Geneva. Adult C57BL/6 mice of the female sex (2 Females) were used in imaging experiments.

Anatomical high-resolution imaging

Accurate prediction of muscle activity during movements is predicated on a sufficient description of the underlying anatomy and physiology. With the goal of creating a predictive model, we began by collecting anatomical data. We obtained 3D scans of mouse forelimbs and trunk musculature through large scale light sheet microscopy imaging of two wild type female mice (11 weeks old). The dataset contains imaging that captured the left distal shoulder and proximal forelimb (Mouse A), the right distal forelimb and paw (Mouse A), and both forelimbs, shoulders, and trunk (Mouse B). Only the left shoulder, trunk, and proximal forelimb were reconstructed in Mouse B. Mouse A and B are different from the four mice used in the empirical reaching dataset with EMG. This imaging dataset provides detailed anatomical information to inform our model development.

Mouse and tissue preparation

Mice were euthanized via subcutaneous injection of pentobarbital. Transcardiac perfusion with saline, followed by 4% paraformaldehyde (PFA) and 0.01% heparin, was performed to preserve tissue integrity. The circulatory system was then washed with saline solution, and the skin was removed. To clear the entire mice, a chamber was set up in the manner that the whole bodies were immersed under the solution which was perfused in a closed loop through the vascular system using a peristaltic pump. All the following incubation steps were performed through this perfusion set up. The bone structures of the mice were decalcified by incubating them in 20% EDTA at 37°C for ten days, with the EDTA solution being renewed every 3 days.

Imaging subjects were pretreated with methanol following the principle of iDISCO+ tissue clearing protocol (Branch et al., 2019; Renier et al., 2014). The tissue was introduced to a gradually increasing concentration of methanol, starting with 20% and increasing by 20% every hour. The clearing chamber was maintained at room temperature. After 5 hours of exposure to methanol, the tissue was chilled at 4° C overnight and then bathed in 66% dichloromethane (DCM) and 33% methanol for 24 hours. The tissue was then bathed twice in 100% methanol for 1 hour before being chilled for 1 hour at 4°C and then transferred into 5% hydrogen peroxide in methanol for 48 hours. Finally, tissue was rehydrated through 1 hour immersion in 80%/60%/40%/20% methanol for one hour per 20% decrement, then transferred to 1x PBS for 24 hours, followed by immersion in a 100ml PBS 10x and 2 ml TritonX-100 solution that was filled to 1L with distillate water. Since only the tissue autofluorescence was targeted for imaging, no antibodies were used in this clearing step process. The tissue was permeabilized with a solution (500 mL) consisting of 400 mL PTx.2, 11.5 g glycine, and 100 mL dimethylsulfoxide (DMSO). The tissue was bathed in solution for 4

days, then transferred to a blocking solution of 42 mL PTx.2, 3 mL donkey serum, and 5 mL DMSO for 3 days. Finally, tissue was washed with 100 mL PBS 10X, 2 mL Tween-20, 1 mL of 10mg/mL heparin, and filled to 1L with distillate water. The tissue was then redehydratedthrough preparation in 20%/40%/60%/80%/100% methanol in 1-hour steps, then bathed in 100% methanol overnight. Afterwards, the tissue was bathed in 66% DCM and 33% methanol for 4 hours, then in 100% DCM for 15 minutes twice, in succession, and finally immersed in DBE solution for imaging.

Imaging parameters

Dissected mouse limbs were arranged in a prone position prior to imaging. Scans were taken with 8.23 um per pixel scans at 8x zoom, with 5 um steps in the z-plane. Imaging was performed using mesoSPIM (Voigt, et al., 2019). Immunostaining was captured in the green channel (488 nm laser) and was imaged using mode tiling wizard with an offset by 75% and a filter set to 530/43. Mouse A's forearms were dissected and imaged in their entirety. Mouse B was imaged from the base of the skull through the joint of the femur and tibia and the entirety of the depth of the sample.

Anatomical segmentation and reconstruction

Muscle segments were manually reconstructed in 3D. We found that muscle density and striation was a sufficient marker of muscles to identify them with light sheet microscopy using the tissue autofluorescence in the green channel, which were enhanced through immunostaining without antibodies (see **Methods: Mouse and tissue preparation**). We used the raw imaging of the mouse anatomy and segmented individual muscles into 3D shape objects using 3D Slicer (Federov et al., 2012) (Fig. 1A). We also segmented the forelimb bones to obtain landmarks and geometries for use in the model. Because not every data set had complete data for the entire forelimb, right and left anatomical datasets were combined through manual alignment in Blender (Blender D.T., 2022). We used anatomical landmarks on the humerus, ulna, and radius to align muscle reconstructions, as these bones were present in all three imagining datasets (left and right forelimbs of mouse A, and whole body of mouse B using the left forelimb). The reconstructions were scaled according to the radius of the bones and confirmed visually by examining the degree of overlap between reconstructions.

Development of a biomechanical model of the mouse forelimb

With a detailed set of reconstructions, we next sought to leverage anatomical descriptions to construct a biomechanical model in OpenSim, a widely-used physics-based modeling and simulation environment used to study movements of humans and other species. The anatomical model was assembled using OpenSim Creator (Kewley et al., 2024). We have also converted the model in MuJoCo (Todorov et al., 2012), but that model was not used for simulations in this study. Each individual muscle's parameters were derived from optical measurements and from previous parameters in Mathewson et al., 2012 and Charles et al., 2016. These were used to set the biophysical properties of the modelled muscles. We used De Groote-Fregly (De Groote et al., 2016) Hill-type muscles within the model, and opted to ignore complex tendon dynamics (i.e., using rigid tendons with no force-length/velocity properties), both to facilitate the production of a functional model and because we did not have access to sufficient data regarding tendon physiology purely from imaging data. Our Hill-type muscles were parametrized by four parameters (maximum isometric force, optimal fiber length, tendon slack length and pennation angle). All these parameters, except for tendon slack length, were determined experimentally in

the muscle dissection study of Mathewson et al., 2012 and through interpolation from known values when a muscle was not described in prior literature. The tendon slack length parameter represents the length where a tendon develops passive elastic force (Uchida & Delp 2021). This parameter cannot be measured experimentally and was set using the optimization procedure of Buchanan et al., 2004, as is commonly performed in the field (Charles et al., 2016), assuming that muscle fibers remain within 0.5 to 1.5 times optimal fiber length throughout the joint's range of motion, which were estimated from both anatomical constraints and video of mouse behavior. Based on the muscle paths from the digital segmentation, we used wrapping surfaces, which are geometric objects in OpenSim, to constrain the muscles to have realistic paths of action. This is necessary for the model to produce realistic moment arms (Charles et al., 2016). We set other parameters in the muscles such as the maximum contraction velocity, the activation time constants and the force-length curves scaled based on prior work on mouse physiology (Charles et al., 2016; see our open-source model for details). We calculated the physiological cross-sectional area (PCSA) by the standard formula developed by Alexander & Vernon (1975), that is, muscle volume divided by fiber length. Muscle fiber pennation angle is set separately in OpenSim models; thus not directly used in PCSA calculations. Bone volume was determined in reconstruction and was uniformly multiplied by a murine bone density scalar (.00425 kg/cm^2), determined from a literature search for empirical measures (Robbins et al., 2018) and prior models of the mouse (Charles et al., 2016), as well as estimations of the center-of-mass and inertia. The resulting model has 21 muscles and 5 bones (along with a composite hand body segment), with the scapula and clavicle serving as fixed position bodies. The model includes four degrees-of-freedom: shoulder elevation, extension, and rotation, as well as elbow flexion. The model is also capable of wrist flexion and rotation, but these degrees-of-freedom were fixed during our simulations. A description of the model geometry is available in Table 1 and the muscle parameterization in Table 2.

Model scaling

Individual mice have variable limb dimensions that models must be altered to accommodate. We accomplished this by using the scale tool in OpenSim to automatically scale the mass, length, and muscle parameters of the model to fit the observed kinematic data originating from a particular mouse subject. We used DeepLabCut (Mathis et al., 2018) to estimate paw, elbow and shoulder markers from video. Our scripts adjusted the marker positions based on a 3D skeletal model with estimated limb lengths (derived from mean inter-marker distances). These adjusted marker positions were then used to scale the OpenSim model to the mouse's proportions.

Mouse behavior

Mouse reaching behavior was recorded from two cameras, spaced 55 degrees apart, and then processed using the DeepLabCut 3D motion tracking software (Mathis et al., 2018). Post-processing of the data parsed the recorded movements into reaching movements. We collected data in a forelimb reaching task and recorded EMG from the biceps brachii, triceps long head, and triceps lateral head in four mice. The activity of three muscles were measured simultaneously with Myomatrix arrays (Zia et al., 2020, Chung et al., 2023), using a bipolar headstage. We estimated the elbow joint angle from the 3D markers. We used the average limb lengths to adjust the DeepLabCut paw, elbow and shoulder markers and ensure that the limb lengths remain constant throughout the video, which is necessary for accurate tracking by the model. Because our forelimb model only has rotational degrees-of-freedom on the shoulder, we could not capture the small translational movement occurring at the shoulder during head-fixed reaching. We subtracted the

shoulder markers displacements from the elbow and paw markers to keep shoulder positional coordinates fixed in our simulations.

The mice underwent two surgeries, 5-7 days apart. First, a head plate was installed to enable head fixation during the experimental training and testing, followed by a second surgery to implant the EMG arrays. Mice were placed on the experimental rig 5-7 days post-EMG implant. Post-surgery, mice were maintained at 80-85% of their initial body weight throughout training and testing phases. For data collection, mice were head-fixed on the experimental rig and trained to perform a single pellet retrieval task (Figs. 1D, 2A). Kinematic measurements and EMG recordings were continuously collected throughout the entire training process, starting from the first session when the mice were completely naive, until they gradually improved and achieved expertise in the task. This training period spanned 11 to 26 sessions, with the mice making their first successful reach (i.e., retrieving a pellet) between 2 to 5 sessions on the rig.

Processed EMG envelopes were normalized to the maximum contraction recording during the session. EMG is usually normalized to the maximum voluntary contractions in studies with human subjects (Kendall et al., 2005). We rectified the EMG signals and then filtered them with a bandpass and lowpass filter suite. We bandpassed the signal from 5 to 500 Hz, rectified the signal, then low-passed further with a cutoff of 10 Hz. Additionally, we normalized the filtered EMG signals with a z-score measure. Each muscle was recorded through 4 leads, but only the qualitatively determined cleanest lead per muscle was used for this study.

Selection of reaches for simulation

Our dataset spanned the entirety of reach training for four mice, and because of the progression of learning, there was natural variance in kinematics performed. We opted to select only from 'expert' mice and to use baseline EMG datasets that were derived from similar reaching kinematics, which eliminated one of the mice. We grouped reaches using the 2-norm metric on 3D paw kinematics to assess similarity, and then selected two sets of ten reaches per mice (n=3), with each set having a different kinematic profile (see Fig. 2C). We enforced expertise by selecting reaches that occurred only after the initial 4 sessions of learning, which was a typical epoch for mice to reach moderate success in reaching. We also compared the optimal control predictions between the early and late sessions of learning. Early sessions were selected from the four mice discussed above (i.e., including the mouse that did not achieve expertise status). Ten reaches were selected from each mouse for the early dataset. Early sessions were restricted to the first 3 sessions of learned reaching.

Optimal control

Optimization of synthetic movements matching empirical kinematics was conducted with direct collocation in Moco (Dembia et al., 2020) as it is well-suited for simulations that track experimental data ("inverse simulations"; e.g., Bishop et al., 2021). Direct collocation enforces the equations-of-motion and physiological relationships as constraints in a nonlinear optimization problem which solves for the states of the musculoskeletal system and the muscle activity over the duration of the simulation. The optimization's objective is to minimize a cost function of two terms: one term that is a proxy for effort (i.e., the sum of muscle activations squared) and one term that represents the tracking cost (i.e., the deviation between the synthesized and the experimental kinematics). The cost function equation is:

$$E = w\mathrm{T}_{\mathrm{paw}} + w\mathrm{T}_{\mathrm{elbow}} + \sum_i a_i^2$$

Here, T_{paw} is the 2-norm squared difference between model and experimental 3D paw coordinates. The experimental coordinates comprised of 100 timepoints during the ballistic phase of reaching. The same holds for T_{elbow}, which is derived from tracking of the mouse elbow position. Term a_i denotes the activation of muscle i in the model and w is a scalar weight set to 10^9 .We optimized over 2500 iterations and 100 mesh points. The simulation was also constrained to start with the joint angles derived during the scaling of the model. The optimization would end early if a convergence tolerance of $1e^{-7}$ was reached. The optimization typically ran for ten minutes on a computer with specifications listed in supplemental Table 1. Rarely, MoCo would not resolve an appropriate kinematic solution for muscle driven simulations (in 2 trials), in which case the cost function was altered to $w = 10^{12}$ then re-simulated.

We compared range normalized predicted muscle activity and EMG measurements using the mean absolute error (MAE) metric at an optimal lag (in a range of –50 to +10 ms; we used a lag of 0 ms for Figure 3 and the late reach set in Figure 4; early reaches had an optimal lag of –50 ms in Figure 4).

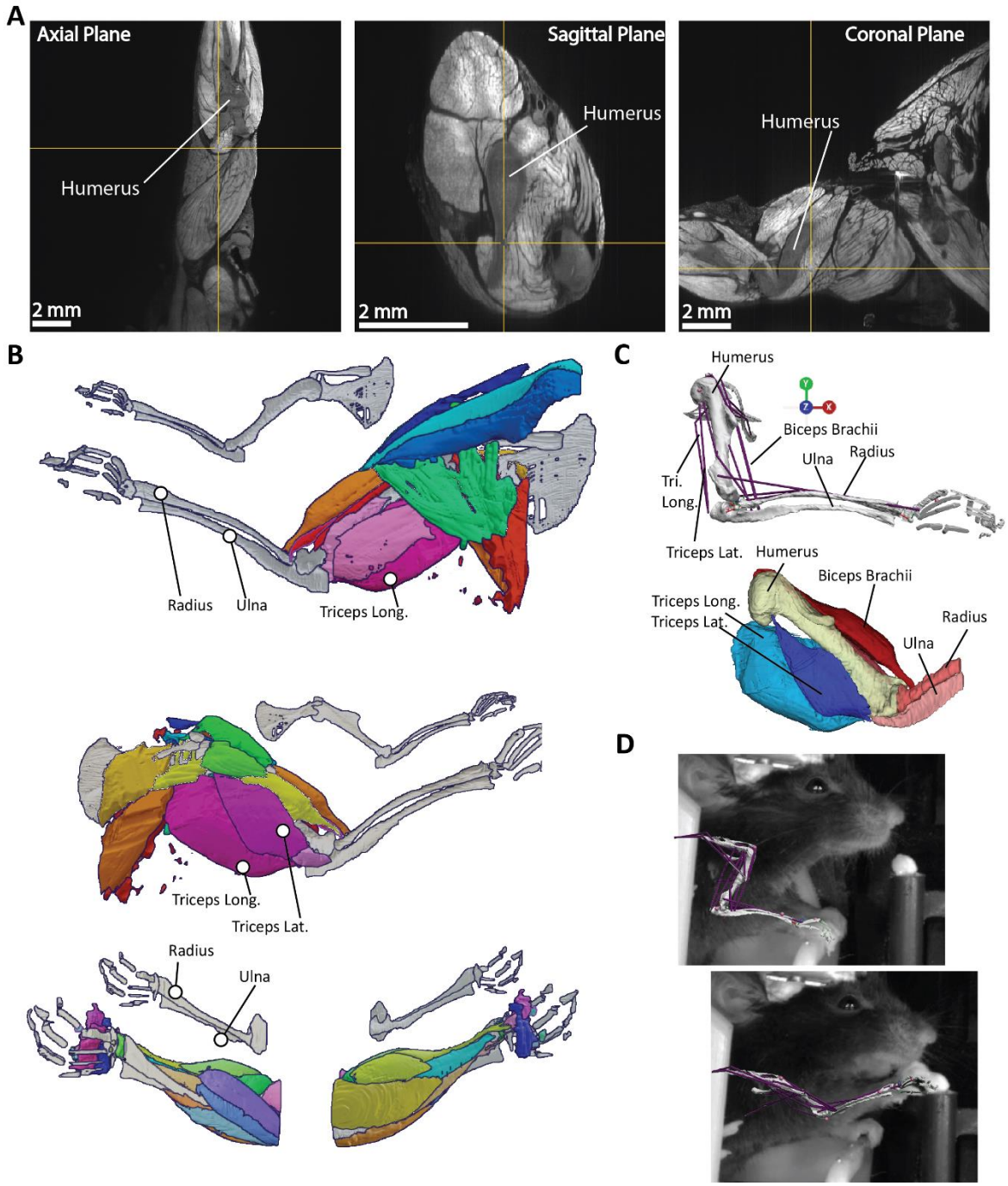

Figure 1. Anatomical reconstruction. A. Optical slices of the mouse forelimb in the axial, sagittal, and coronal planes. The mouse arm is oriented in the prone position. Labels added to highlight prominent muscles as an example of a reconstruction target. **B.** 3D projections of optical tracing results as a composite across mice. Upper panels show composite scan, while lower panels show the left hand of mouse A to highlight density of wrist-inserting muscles. 3D projections show morphology and attachment sites of muscles on bones that were used to create biophysical model. **C.** Biomechanical model (OpenSim) reconstruction developed from the 3D projections. **D.** Biomechanical model projection on video images taken from of a mouse reaching.

RESULTS

Kinematic Tracking

We tasked the physiological forelimb model to track recorded DeepLabCut-tracked kinematics using optimal control algorithms (see **Methods: Optimal control)**. The model was scaled and then optimized with direct collocation to track the paw and elbow across the ballistic epoch of the reach (Fig. 2 AB). Animals have natural variance in produced reaching movements and motor control, so we opted to group six sets of ten reaches by their kinematic similarity across time (Fig. 2C; see **Methods: Selection of reaches for simulation)**. We deliberately selected these sets of varying reaching kinematics to explore the ability of the model to predict varied motor behaviors. We were able to recreate limb kinematics with low error, with the majority of synthesized kinematics per timestep falling within 1 standard deviation of the empirical kinematic mean (Fig. 2D, blue violin plots; N = 60 reaches) across the x, y, and z dimensions of the paw and elbow trajectories.

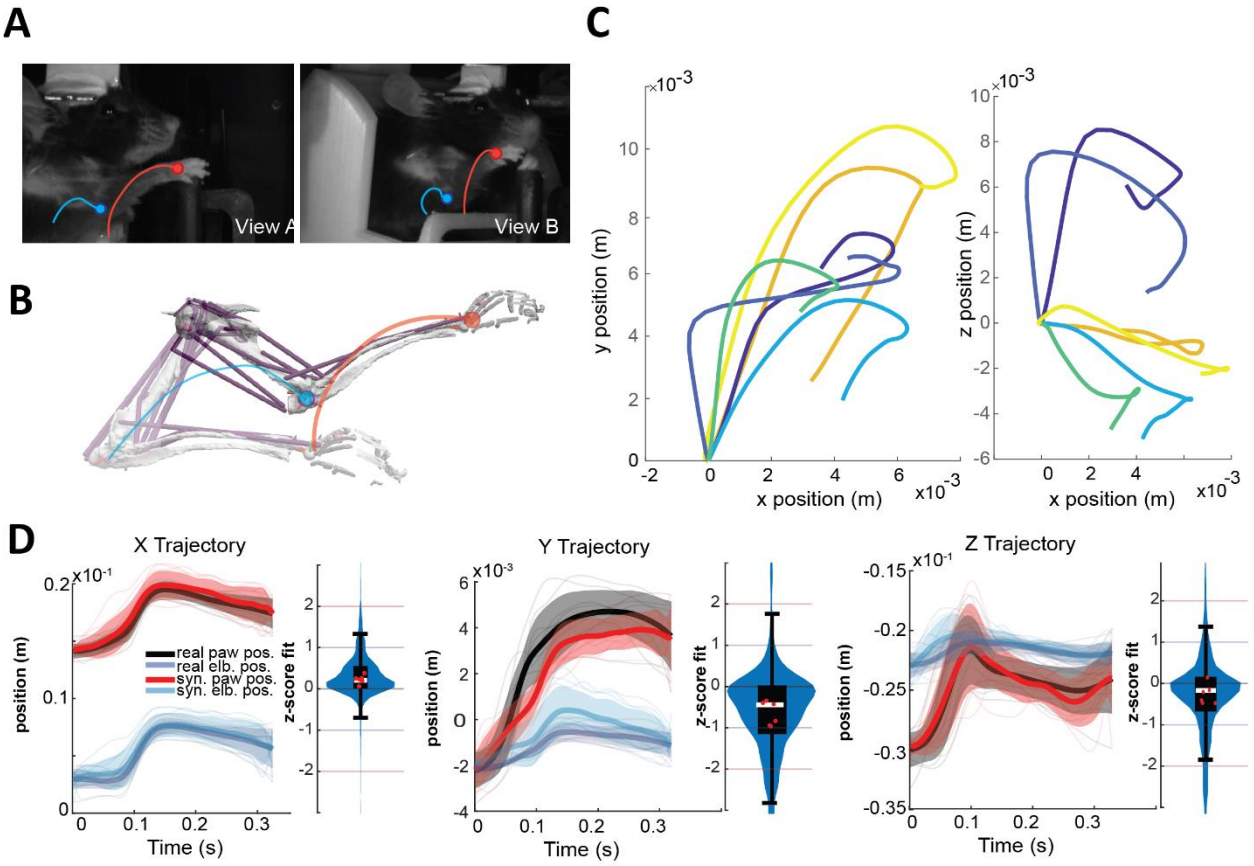

Figure 2. A. Example video screenshots with schematic elbow and paw marker trajectories. **B.** A biomechanical model with virtual markers on the elbow and paw. An optimal control problem is solved to minimize the difference between the virtual and empirical markers. **C.** Means of six sets of reaches selected for simulation, with the x vs y (forward vs vertical) dimensions plotted on the left and x vs z (forward vs lateral) on the right. **D.** Mean and standard deviation of 60 reaches for the empirical and synthesized marker trajectories. The z-score of the synthesized markers are largely within 1 standard deviation (see violin plots in blue), and the means per set of ten reaches are all within 1 standard deviation (red dots). Black box plots denote median (white bar), 25 to 75th percentile distributions (black box), and 10th to 90th percentile distributions (short horizontal black lines).

Model muscle activity patterning for reaching movements

We next tasked the model to synthesize muscle activity during reaching movements with optimal control in order to predict the muscle excitations that underlie observed kinematics. The predictions were not trained with 'ground truth' or empirical muscle activity. As shown in the examples in Fig. 3A, we observe that the mean synthesized muscle activity closely resembles empirical muscle activity over the duration of the reach for all three muscles. We measure the performance of the model via the mean absolute error (MAE) of normalized ground truth EMG signals from model signals. The mean muscle excitations produced by the model were typically within a single standard deviation of the experimental EMG activity (Fig. 3B, red dots in violin plots; between 50-57 of the 60 reaches, depending on the mice and assayed muscle).

On a reach-by-reach basis, the muscle excitations produced by the model across all time points were typically within two standard deviations of the experimental EMG activity, suggesting that, while still relatively accurate, individual reaches are more difficult to accurately predict. Paired reach-to-reach predictions were likely less accurate because mice were highly variable in their muscle patterning, even between reaches with the same kinematic profile (Supp. Fig 1). Some of the observed muscle patterning may be energetically inefficient, more consistent with early learning or motor exploration, which would not be predicted as accurately by optimal control approaches. In Fig. 3C, we show that the mean model EMG predictions outperform the shuffled experimental EMG data (i.e., having the same distribution as the ground truth EMG; two-sided t-test, biceps $p = 3.1e-6$, triceps long head $p = 2.7e-6$, triceps lateral head $p = 2.3e-3$.; P-values were Holm-Bonferroni corrected for multiple comparisons, $N = 60$ shuffled trials and six synthesized means).

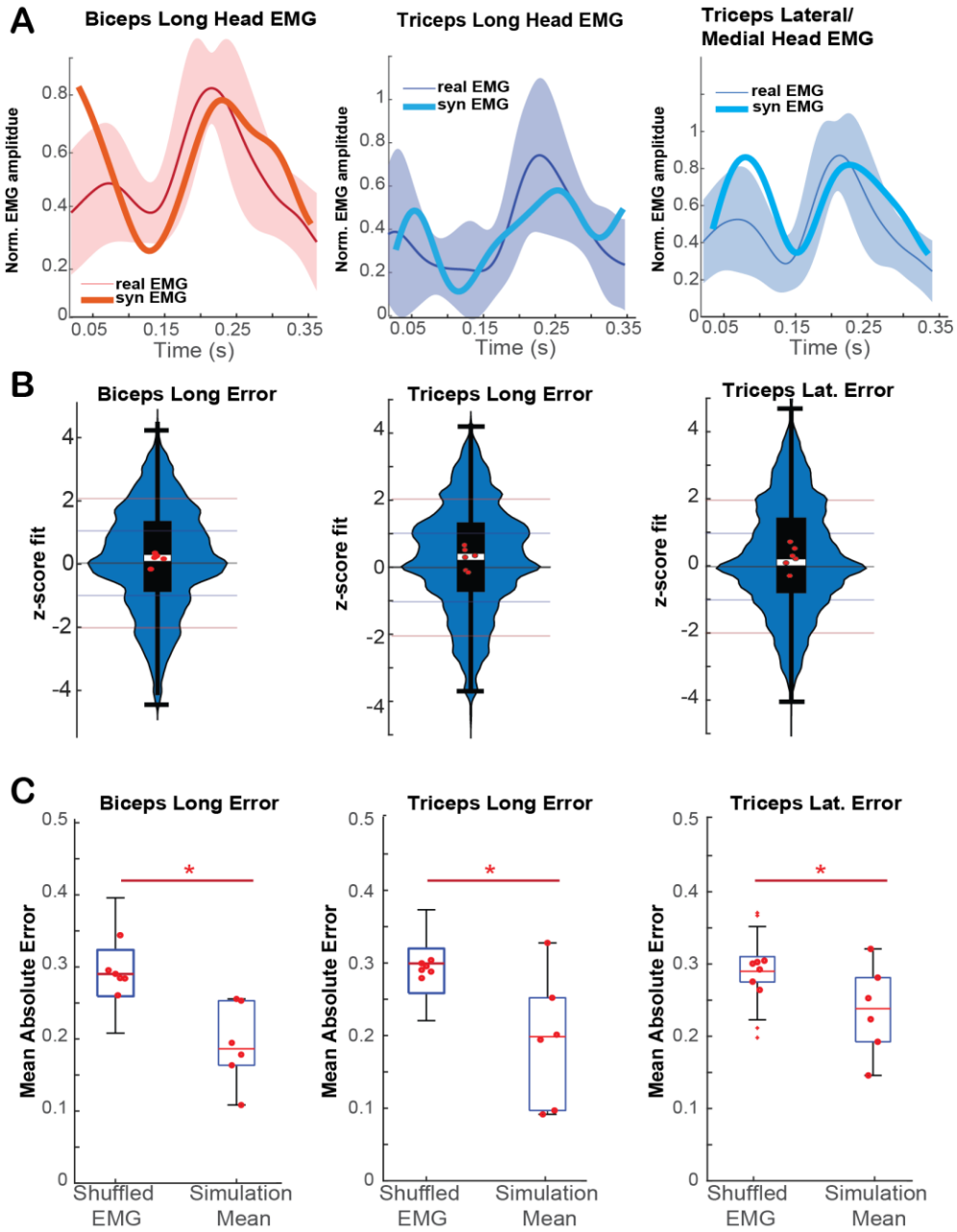

Figure 3. **A.** Comparisons of synthesized muscle excitations and experimental EMG activity. Curves show means and standard deviations (line and shaded region) of ten reaches with similar experimental elbow and paw trajectories that were chosen from mouse behavior dataset. The mean synthesized excitations are shown in thick red for biceps long head, thick cyan for triceps long head, and thick blue for triceps medial head compared to the base lateral head activity. **B.** Violin plots including the entire dataset of 60 reaches. The mean synthesized muscle activity lies largely within 1 standard deviation of mean experimental muscle activity (red dots). On a reach-by-reach basis, the synthesized muscle activity lies largely within a z-score of 2 standard deviations (blue violin plots). Black box plots denote median z-deviation (white bar), 25 to 75th percentile distributions (black box), and 10th to 90th percentile distributions (horizontal black line). **C.** A comparison of mean absolute error between time-shuffled physiological EMG data and synthetic excitation means to the real mean of the tracked data. Synthetic excitation means have lower MAE than the time-shuffled data in all three muscles recorded (two-sided t-test, biceps p = 3.1e-6, triceps long head p = 2.7e-6, triceps lateral head p =2.4e-3. P-values were Holm-Bonferroni corrected for multiple comparisons). Black box plots denote median (red horizonal bar), 25 to 75th percentile distributions (black box), and 10th to 90th percentile distributions (short horizontal black lines and stems).

Mouse motor learning and optimal control

The progression of reach kinematics and muscle patterning in mice learning a novel task is a relatively understudied phenomenon, especially given the paucity of experimental approaches to studying whole-limb muscle activity. We leveraged our model's explanatory power to investigate the possibility that mice approach an optimal motor control solution during the progression of training by evaluating optimal control predictions during early and late sessions of training. In Fig. 3, we compared the optimal control predictions with reaches selected from expert mice (i.e., after at least 5 sessions of successful reaching). In Fig. 4, we compared how the optimal control predictions varied when the reaches were chosen in the early (i.e., in the first 3 sessions after the first successful reach to pellet) or late stages of learning. We found that mice tended to use muscle excitation patterns that converged more closely to those derived from optimal control in the later stages of learning. These results were significant when pooling the data across all recorded EMG channels but not on individual channels, likely because of our small sample size (early N = 4, late N = 6 for means comparisons, early N = 40, late N = 60 for trial-to-trial comparisons shown in Fig. 4. Comparison of trial-to-trial data was compared with a two-sided t-test with a p-value of 3.5e-6).

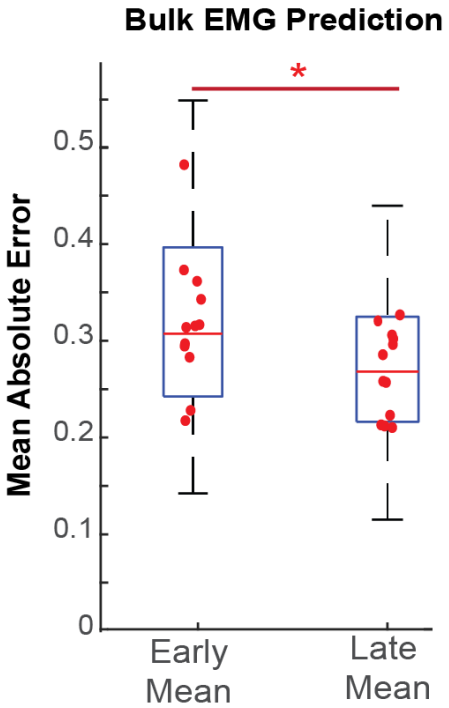

Figure 4. A comparison of the utility of the simulated muscle excitations in predicting EMG during early or late training sessions (i.e. the first three sessions after the first successful reaches being *early* and sessions later than four sessions after the initial successful reach being *late*.) Late reaches, on bulk, have a significantly lower mean absolute error than early sessions (two-sided t-test, p = 3.5e-6, early N = 40, late N = 60) for predicting trial-to-trial EMG activity. Black box plots denote median (red horizonal bar), 25 to 75th percentile distributions (black box), and 10th to 90th percentile distributions (short horizontal black lines and stems).

DISCUSSION

Mouse models are widely used to study the neural control of movement, motor disorders, muscle physiology and develop novel brain-computer interfaces and neurotechnologies. Despite the widespread use of mice in the health sciences, the only available biomechanical model of the mouse forelimb is based largely on educated guesses, which could lead to inaccurate kinematics and muscle activity predictions. We used high-detail anatomical reconstruction from large scale light sheet microscopy scans to develop the first physiological biomechanical model of the mouse forelimb in terms of musculoskeletal geometry and muscle architecture (Mathewson et al., 2012). Traditional dissection methods were deemed impractical to determine the musculoskeletal geometry because of the small size of the mouse forelimb, especially in determining the attachment points of the tendons of the elbow. Other imaging techniques such as microCT would have likely also been adequate to produce sufficient soft tissue contrast for the reconstruction (Charles et al., 2016). We used this biomechanical model with optimal control to synthesize muscle coordination patterns that produce reaching movements in simulations that match experimental kinematics. Accurately predicting muscle activity is challenging because of the infinite possible coordination patterns consistent with the tracked experimental kinematics and the high physiological variance in the patterns observed in real mice (i.e., for very similar kinematics, mice often use very different muscle patterning strategies, some of which may be energetically costly, have high or low co-contraction, be robust to disturbances, etc.; Supplemental Figure 1). Our optimal control cost function only has terms to encourage low energy (via the sum of muscle activations squared proxy) and producing kinematics consistent with experimental kinematics. Therefore, we would not expect the optimal control predictions to closely match the experimental muscle activity on a reach-by-reach basis because of the high variability in the experimental muscle patterning data. Nevertheless, we found that the mean optimal control muscle activity predictions have strong resemblance with the mean empirical muscle activity (Fig. 3A). These results held for all three recorded muscles with EMG (biceps, triceps long head and triceps lateral head). To the best of our knowledge, this is the first work in any species, including humans, showing resemblance between synthesized and experimental muscle activity for three-dimensional reaching movements with a biomechanical model.

Neuroscience experiments are sometimes limited in scope by the difficulty of simultaneous recording of behavior, neurological signals, and, in some cases, muscle activity. Multisite muscle recordings are limited to accessible sites, and this limitation is exacerbated in mice, where access to and implantation of many muscles is often infeasible. This model is meant to supplement experiments where knowledge of muscle activity patterning could bring insight about the nature of neural activity patterning. Scientists with behavioral data can extract an estimate of whole-forelimb muscle activity from the model given a set of kinematics over time. Tracking of mouse kinematics has become broadly accessible through the advent of pose-based tracking software like DeepLabCut, which was used in the present study to monitor limb position during reaching behaviors (Mathis et al., 2018). The conjunction of tracking and synthesis of whole-forelimb muscle activations promises to expand research into behavioral control significantly.

There are several extensions to our biomechanical model and computational tools possible for future work. Our computational tools assume that no EMG is available during the experiments. If EMG is collected during the experiment, the optimal control problem can be solved to predict the muscle activity of muscles without EMG recordings while matching experimental EMG and kinematics data in tracking simulations (Dembia et al., 2021). It is also possible to change the cost function in the optimal control problem and produce predictive simulations that do not require any

experimental data, including kinematics, by specifying goals constrained only to endpoint or end-state of the limb. The optimal control problem could then predict the reaching kinematics and muscle activity when there is a change in the task (e.g., a new pellet location) or limb biomechanics (e.g., a weight placed on the forelimb). This model might also be used to assay disease states to expand on known motor symptoms, such as enforced variability in endpoint accuracy as seen in cerebellar disease (Bonnefoi-Kyriacou et al., 2018), forced variation in muscle coordination patterns such as those seen after stroke (Cheung et al., 2012) or replications of impaired kinematics in Parkinson's disease (Vissani et al., 2021).

While the model evaluation in this study focuses on reaching movements, which are commonly used to assess motor control across species, the insights gained extend beyond this specific task. Reaching movements provide a well-studied framework for understanding motor coordination, but motor systems are capable of generating numerous possible muscle coordination patterns for any given movement (Harris & Wolpert 1998). Optimal control chooses the muscle excitation pattern that achieves task constraints, while minimizing a proxy for effort or energy (e.g., the sum of muscle activations squared) and possibly other terms (Al Borno et al., 2020). We apply optimal control to predict an energetically efficient muscle activity pattern that achieves the reaching kinematics task. This study is focused on the ballistic phase of reaching movements, and we did not model the grasping phase during the reach as we would have needed to include the muscles that control the wrist and fingers in the model and simulate interaction with the pellet. One additional discrepancy between our simulation and the empirical reach is that mice, before starting their reach, rested their paws on a bar, which we did not simulate (and may impact the predicted muscle activity at the start of the ballistic phase).

Our simulations were evaluated with head-fixed mouse reaching. Using the biomechanical model in free-reaching mice may be less accurate because it has more significant scapular movements, which we assume to stay fixed in our model. In future work, researchers could either add a degree-of-freedom and a joint motor to allow translational movement of the scapula or incorporate the muscles that control the scapula as a free body in the biomechanical model. The optimal control solutions produce open-loop muscle coordination patterns that are not responsive to noise or changing task or environmental constraints. It is, however, possible to develop closed-loop controllers to track the optimized trajectory or to develop feedback controllers with reinforcement learning or introduce stochastic noise representing imprecise neural controls (e.g., Van Wouwe et al., 2022). Finally, we generalized our muscle parameterization to past work and observations from other small mammals (Powell et al. 1984), but the model would certainly benefit from a thorough investigation of the murine forelimb's muscles through dissection and testing, which was beyond the scope of our study.

We make our computational tools freely available as open-source. We have written custom code to convert our OpenSim model into the MuJoCo physics simulation environment (Todorov et al., 2012). Although the model is available in MuJoCo, the computational tools for optimal control are based in OpenSim; therefore, MuJoCo users will need to develop their own code to produce the simulations with the model. While the model evaluation in this study focuses on reaching movements, our tools can be used to predict muscle activity in other forelimb movements. Users of our computational tools should note that the optimal control predictions are expected to more closely resemble empirical muscle activity on a mean-basis rather than on a trial-by-trial basis and carry the assumption of closely matched kinematics. Furthermore, the predictions are expected to improve when mice have learned to perform the task well as opposed to when mice are still in the early stages of learning. Nevertheless, the model predictions in the early stages of

learning are still within one standard deviation of empirical results and represent a significant improvement over randomized guesses from the naturalistic EMG distribution. An exciting use case for our biomechanical model is to control it with artificial neural networks and relate the activity in these networks with empirical neural activity from system neuroscience laboratories (Aldarondo et al., 2024). Combining our computational tools and experimental data could lay the foundations for future studies elucidating the principles that drive the control of movement.

ACKNOWLEDGEMENTS

JIG designed the study, wrote the manuscript, assembled the model, and performed analysis. AGC performed imaging and prepared mice under the supervision of DH. . SKC designed the behavioral experiment, performed the headplate and EMG surgeries, trained the mice, recorded electromyography, and provided datasets under the supervision of AP. JH helped design and conceptualize the study. MAB designed the study, wrote the manuscript, provided tools for analysis and supervised the study. We thank InWorks at CU Denver for imaging and segmentation. The behavioral study included in this work was supported by NIH grants (along with Simons Consortium): U24NS126936 and R01NS109237. JIG was supported by NLM grants 2T15LM009451-16 and 5T15LM009451-15.

REFERENCES

1. Al Borno, M., Vyas, S., Shenoy, K. V., & Delp, S. L. (2020). High-fidelity musculoskeletal modeling reveals that motor planning variability contributes to the speed-accuracy tradeoff. eLife, 9, e57021. https://doi.org/10.7554/eLife.57021

2. Aldarondo, D., Merel, J., Marshall, J. D., Hasenclever, L., Klibaite, U., Gellis, A., Tassa, Y., Wayne, G., Botvinick, M., & Ölveczky, B. P. (2024). A virtual rodent predicts the structure of neural activity across behaviours. Nature, 632(8025), 594–602. https://doi.org/10.1038/s41586-024-07633-4

3. Becker, M. I., Calame, D. J., Wrobel, J., & Person, A. L. (2020). Online control of reach accuracy in mice. Journal of Neurophysiology, 124(6), 1637–1655. https://doi.org/10.1152/jn.00324.2020

4. Becker, M. I., & Person, A. L. (2019). Cerebellar Control of Reach Kinematics for Endpoint Precision. Neuron, 103(2), 335-348.e5. https://doi.org/10.1016/j.neuron.2019.05.007

5. Blender Development Team. (2022). Blender (Version 3.2.2) [Computer software]. https://www.blender.org

6. Bollu, T., Whitehead, S. C., Prasad, N., Walker, J., Shyamkumar, N., Subramaniam, R., Kardon, B., Cohen, I., & Goldberg, J. H. (2019). Automated home cage training of mice in a hold-still center-out reach task. Journal of Neurophysiology, 121(2), 500–512. https://doi.org/10.1152/jn.00667.2018

7. Bonnefoi-Kyriacou, B., Legallet, E., Lee, R. G., & Trouche, E. (1998). Spatio-temporal and kinematic analysis of pointing movements performed by cerebellar patients with limb ataxia. Experimental Brain Research, 119(4), 460–466. https://doi.org/10.1007/s002210050361

8. Buchanan TS, Lloyd DG, Manal K, Besier TF. Neuromusculoskeletal modeling: estimation of muscle forces and joint moments and movements from measurements of neural command. J Appl Biomech. 2004 Nov;20(4):367-95. doi: 10.1123/jab.20.4.367. PMID: 16467928; PMCID: PMC1357215.

9. Burgess, C. P., Lak, A., Steinmetz, N. A., Zatka-Haas, P., Bai Reddy, C., Jacobs, E. A. K., Linden, J. F., Paton, J. J., Ranson, A., Schröder, S., Soares, S., Wells, M. J., Wool, L. E., Harris, K. D., & Carandini, M. (2017). High-Yield Methods for Accurate Two-Alternative Visual Psychophysics in Head-Fixed Mice. Cell Reports, 20(10), 2513–2524. https://doi.org/10.1016/j.celrep.2017.08.047

10. Burkholder, T. J., Fingado, B., Baron, S., & Lieber, R. L. (1994). Relationship between muscle fiber types and sizes and muscle architectural properties in the mouse hindlimb. Journal of Morphology, 221(2), 177–190. https://doi.org/10.1002/jmor.1052210207

11. Calame, D. J., Becker, M. I., & Person, A. L. (2023). Cerebellar associative learning underlies skilled reach adaptation. Nature Neuroscience, 26(6), 1068–1079. https://doi.org/10.1038/s41593-023-01347-y

12. Charles, J. P., Cappellari, O., Spence, A. J., Hutchinson, J. R., & Wells, D. J. (2016). Musculoskeletal Geometry, Muscle Architecture and Functional Specialisations of the Mouse Hindlimb. PLOS ONE, 11(4), e0147669. https://doi.org/10.1371/journal.pone.0147669

13. Cheung, V. C. K., Turolla, A., Agostini, M., Silvoni, S., Bennis, C., Kasi, P., Paganoni, S., Bonato, P., & Bizzi, E. (2012). Muscle synergy patterns as physiological markers of motor cortical damage. Proceedings of the National Academy of Sciences, 109(36), 14652–14656. https://doi.org/10.1073/pnas.1212056109

14. Chung B, Zia M, Thomas KA, Michaels JA, Jacob A, Pack A, Williams MJ, Nagapudi K, Teng LH, Arrambide E, Ouellette L, Oey N, Gibbs R, Anschutz P, Lu J, Wu Y, Kashefi M, Oya T, Kersten R, Mosberger AC, O'Connell S, Wang R, Marques H, Mendes AR, Lenschow C, Kondakath G, Kim JJ, Olson W, Quinn KN, Perkins P, Gatto G, Thanawalla A, Coltman S, Kim T, Smith T, Binder-Markey B, Zaback M, Thompson CK, Giszter S, Person A, Goulding M, Azim E, Thakor N, O'Connor D, Trimmer B, Lima SQ, Carey MR, Pandarinath C, Costa RM, Pruszynski JA, Bakir M, Sober SJ. Myomatrix arrays for high-definition muscle recording. Elife. 2023 Dec 19;12:RP88551. doi: 10.7554/eLife.88551. PMID: 38113081; PMCID: PMC10730117.

15. Conner, J. M., Bohannon, A., Igarashi, M., Taniguchi, J., Baltar, N., & Azim, E. (2021). Modulation of tactile feedback for the execution of dexterous movement. Science, 374(6565), 316–323. https://doi.org/10.1126/science.abh1123

16. De Groote, F., Kinney, A. L., Rao, A. V., & Fregly, B. J. (2016). Evaluation of Direct Collocation Optimal Control Problem Formulations for Solving the Muscle Redundancy Problem. Annals of Biomedical Engineering, 44(10), 2922–2936. https://doi.org/10.1007/s10439-016-1591-9

17. Deisseroth, K., Feng, G., Majewska, A. K., Miesenböck, G., Ting, A., & Schnitzer, M. J. (2006). Next-Generation Optical Technologies for Illuminating Genetically Targeted Brain Circuits. The Journal of Neuroscience, 26(41), 10380–10386. https://doi.org/10.1523/JNEUROSCI.3863-06.2006

18. DeLaurier, A., Burton, N., Bennett, M., Baldock, R., Davidson, D., Mohun, T. J., & Logan, M. P. (2008). The Mouse Limb Anatomy Atlas: An interactive 3D tool for studying embryonic limb patterning. BMC Developmental Biology, 8(1), 83. https://doi.org/10.1186/1471-213X-8-83

19. Dembia, C. L., Bianco, N. A., Falisse, A., Hicks, J. L., & Delp, S. L. (2020). OpenSim Moco: Musculoskeletal optimal control. PLOS Computational Biology, 16(12), e1008493. https://doi.org/10.1371/journal.pcbi.1008493

20. Dogdas, B., Stout, D., Chatziioannou, A. F., & Leahy, R. M. (2007). Digimouse: A 3D whole body mouse atlas from CT and cryosection data. Physics in Medicine and Biology, 52(3), 577–587. https://doi.org/10.1088/0031-9155/52/3/003

21. Fedorov, A., Beichel, R., Kalpathy-Cramer, J., Finet, J., Fillion-Robin, J.-C., Pujol, S., Bauer, C., Jennings, D., Fennessy, F., Sonka, M., Buatti, J., Aylward, S., Miller, J. V., Pieper, S., & Kikinis, R. (2012). 3D Slicer as an image computing platform for the

Quantitative Imaging Network. Magnetic Resonance Imaging, 30(9), 1323–1341. https://doi.org/10.1016/j.mri.2012.05.001

22. Fleischer, P., Abbasi, A., Fealy, A. W., Danielsen, N. P., Sandhu, R., Raj, P. R., & Gulati, T. (2023). Emergent Low-Frequency Activity in Cortico-Cerebellar Networks with Motor Skill Learning. Eneuro, 10(2), ENEURO.0011-23.2023. https://doi.org/10.1523/ENEURO.0011-23.2023

23. Galiñanes, G. L., Bonardi, C., & Huber, D. (2018). Directional Reaching for Water as a Cortex-Dependent Behavioral Framework for Mice. Cell Reports, 22(10), 2767–2783. https://doi.org/10.1016/j.celrep.2018.02.042

24. Habart M, Lio G, Soumier A, Demily C, Sirigu A. An optimized iDISCO+ protocol for tissue clearing and 3D analysis of oxytocin and vasopressin cell network in the developing mouse brain. STAR Protoc. 2023 Mar 17;4(1):101968. doi: 10.1016/j.xpro.2022.101968. Epub 2023 Jan 3. PMID: 36598854; PMCID: PMC9826885.

25. Harris, C. M., & Wolpert, D. M. (1998). Signal-dependent noise determines motor planning. Nature, 394(6695), 780–784. https://doi.org/10.1038/29528

26. Hebel, R., & Stromberg, M. W. (1986). Anatomy and embryology of the laboratory rat. BioMed Verl.

27. Iwaniuk, A. N., & Whishaw, I. Q. (2000). On the origin of skilled forelimb movements. Trends in Neurosciences, 23(8), 372–376. https://doi.org/10.1016/S0166-2236(00)01618-0

28. Kendall, F. P., McCreary, E. K., Provance, P. G., Rodgers, M. M., and Romani, W. A. (2005). *Muscles: Testing and Function, with Posture and Pain (Kendall, Muscles)*. Philadelphia, PA: Lippincott Williams and Wilkins.

29. Kewley, A., Beesel, J., & Seth, A. (2024). OpenSim Creator (Version 0.5.12) [Computer software]. Zenodo. https://doi.org/10.5281/ZENODO.11086325

30. Khanna, P., Totten, D., Novik, L., Roberts, J., Morecraft, R. J., & Ganguly, K. (2021). Low-frequency stimulation enhances ensemble co-firing and dexterity after stroke. Cell, 184(4), 912-930.e20. https://doi.org/10.1016/j.cell.2021.01.023

31. Mathewson, M. A., Chapman, M. A., Hentzen, E. R., Fridén, J., & Lieber, R. L. (2012). Anatomical, architectural, and biochemical diversity of the murine forelimb muscles. Journal of Anatomy, 221(5), 443–451. https://doi.org/10.1111/j.1469-7580.2012.01559.x

32. Mathis, A., Mamidanna, P., Cury, K. M., Abe, T., Murthy, V. N., Mathis, M. W., & Bethge, M. (2018). DeepLabCut: Markerless pose estimation of user-defined body parts with deep learning. Nature Neuroscience, 21(9), 1281–1289. https://doi.org/10.1038/s41593-018-0209-y

33. Navarro, M., Ruberte, J., & Carretero, A. (2017). Myology. In Morphological Mouse Phenotyping (pp. 63–88). Elsevier. https://doi.org/10.1016/B978-0-12-812972-2.50004-0

34. Powell, P. L., Roy, R. R., Kanim, P., Bello, M. A., & Edgerton, V. R. (1984). Predictability of skeletal muscle tension from architectural determinations in guinea pig hindlimbs. Journal of Applied Physiology, 57(6), 1715–1721. https://doi.org/10.1152/jappl.1984.57.6.1715

35. Renier N, Wu Z, Simon DJ, Yang J, Ariel P, Tessier-Lavigne M. iDISCO: a simple, rapid method to immunolabel large tissue samples for volume imaging. Cell. 2014 Nov 6;159(4):896-910. doi: 10.1016/j.cell.2014.10.010. Epub 2014 Oct 30. PMID: 25417164.

36. Robbins, A., Tom, C. A. T. M. B., Cosman, M. N., Moursi, C., Shipp, L., Spencer, T. M., Brash, T., & Devlin, M. J. (2018). Low temperature decreases bone mass in mice: Implications for humans. American Journal of Physical Anthropology, 167(3), 557–568. https://doi.org/10.1002/ajpa.23684

37. Sauerbrei, B. A., Guo, J.-Z., Cohen, J. D., Mischiati, M., Guo, W., Kabra, M., Verma, N., Mensh, B., Branson, K., & Hantman, A. W. (2020). Cortical pattern generation during dexterous movement is input-driven. Nature, 577(7790), 386–391. https://doi.org/10.1038/s41586-019-1869-9

38. Serradj, N., Marino, F., Moreno-López, Y., Bernstein, A., Agger, S., Soliman, M., Sloan, A., & Hollis, E. (2023). Task-specific modulation of corticospinal neuron activity during motor learning in mice. Nature Communications, 14(1), 2708. https://doi.org/10.1038/s41467-023-38418-4

39. Seth, A., Hicks, J. L., Uchida, T. K., Habib, A., Dembia, C. L., Dunne, J. J., Ong, C. F., DeMers, M. S., Rajagopal, A., Millard, M., Hamner, S. R., Arnold, E. M., Yong, J. R., Lakshmikanth, S. K., Sherman, M. A., Ku, J. P., & Delp, S. L. (2018). OpenSim: Simulating musculoskeletal dynamics and neuromuscular control to study human and animal movement. PLOS Computational Biology, 14(7), e1006223. https://doi.org/10.1371/journal.pcbi.1006223

40. Seth, A., Matias, R., Veloso, A. P., & Delp, S. L. (2016). A Biomechanical Model of the Scapulothoracic Joint to Accurately Capture Scapular Kinematics during Shoulder Movements. PLOS ONE, 11(1), e0141028. https://doi.org/10.1371/journal.pone.0141028

41. Tata Ramalingasetty, S., Danner, S. M., Arreguit, J., Markin, S. N., Rodarie, D., Kathe, C., Courtine, G., Rybak, I. A., & Ijspeert, A. J. (2021). A Whole-Body Musculoskeletal Model of the Mouse. IEEE Access, 9, 163861–163881. https://doi.org/10.1109/ACCESS.2021.3133078

42. Todorov, E., Erez, T., & Tassa, Y. (2012). MuJoCo: A physics engine for model-based control. 2012 IEEE/RSJ International Conference on Intelligent Robots and Systems, 5026–5033. https://doi.org/10.1109/IROS.2012.6386109

43. Uchida, T. K., Delp, S., & Delp, D. B. (2020a). Biomechanics of movement: The science of sports, robotics, and rehabilitation. The MIT Press.

44. Van Wouwe, T., Ting, L. H., & De Groote, F. (2022). An approximate stochastic optimal control framework to simulate nonlinear neuro-musculoskeletal models in the presence of noise. PLOS Computational Biology, 18(6), e1009338. https://doi.org/10.1371/journal.pcbi.1009338

45. Vissani, M., Palmisano, C., Volkmann, J., Pezzoli, G., Micera, S., Isaias, I. U., & Mazzoni, A. (2021). Impaired reach-to-grasp kinematics in parkinsonian patients relates to dopamine-dependent, subthalamic beta bursts. Npj Parkinson's Disease, 7(1), 53. https://doi.org/10.1038/s41531-021-00187-6

46. Voigt, F. F., Kirschenbaum, D., Platonova, E., Pagès, S., Campbell, R. A. A., Kastli, R., Schaettin, M., Egolf, L., Van Der Bourg, A., Bethge, P., Haenraets, K., Frézel, N., Topilko, T., Perin, P., Hillier, D., Hildebrand, S., Schueth, A., Roebroeck, A., Roska, B., … Helmchen, F. (2019). The mesoSPIM initiative: Open-source light-sheet microscopes for imaging cleared tissue. Nature Methods, 16(11), 1105–1108. https://doi.org/10.1038/s41592-019-0554-0

47. Wagner, M. J., Kim, T. H., Kadmon, J., Nguyen, N. D., Ganguli, S., Schnitzer, M. J., & Luo, L. (2019). Shared Cortex-Cerebellum Dynamics in the Execution and Learning of a Motor Task. Cell, 177(3), 669-682.e24. https://doi.org/10.1016/j.cell.2019.02.019

48. Yang, W., Kanodia, H., & Arber, S. (2023). Structural and functional map for forelimb movement phases between cortex and medulla. Cell, 186(1), 162-177.e18. https://doi.org/10.1016/j.cell.2022.12.009

49. Zia, M., Chung, B., Sober, S., & Bakir, M. S. (2020). Flexible Multielectrode Arrays With 2-D and 3-D Contacts for In~ Vivo Electromyography Recording. IEEE Transactions on Components, Packaging and Manufacturing Technology, 10(2), 197–202. https://doi.org/10.1109/TCPMT.2019.2963556

Table 1. Muscle origins and insertions.

Muscle Name	Origin Parent-Body	Origin Coordinates (m)	Insertion Parent-Body	Insertion Coordinates (m)
Anconeus	Humerus	[5.2e-3, 5e-4, 1.07e-2]	Ulna	[2.4e-3, -2e-4, 8.8e-3]
Anconeus, Short Head	Humerus	[3.6e-3, -9e-4, 9.1e-3]	Ulna	[3.8e-3, -6e-4, 8.3e-3]
Biceps, Long Head	Scapula	[8.5-3, 2.3e-2,1.2e-2]	Ulna	[2.1e-3, 4.9e-5, 8.8e-3]
Biceps, Short Head	Humerus	[9.1e-3, 1.5e-3,1.2e-2]	Ulna	[2.1e-3, 9.8e-5, 8.8e-3]
Brachialis, Proximal Head	Humerus	[2.3e-3, 5.9e-5, 8.8e-3]	Ulna	[2.2-3, 5.9e-5, 8.8e-3]
Brachialis, Distal Head	Humerus	[8.2e-3, 1.4e-3, 1.2e-2]	Ulna	[2.2-3, 5.9e-5, 8.8e-3]
Brachioradialis	Humerus	[4e-3, 6.5e-4, 9.1e-3]	Radius	[-3e-3, 1.3e-3, 1.2e-2]
Deltoid, Medial	Clavicle	[9.3e-3. 5e-4, 1.3e-2]	Humerus	[5.5e-3, 1.2e-3, 1.2e-2]
Deltoid, Posterior	Scapula	[8.7e-3, 1.2e-3, 1.2e-2]	Humerus	[5.9e-3, 1.5e-3, 1.1e-2]
Flexorcarpiradialis	Humerus	[3.4e-3, -9.3e-4, 9.2e-3]	Hand	[-4e-3, 1.6e-3, 1.2e-2]
Infraspinatus	Scapula	[1.1e-2, 1.3e-3, 1.2e-2]	Humerus	[8.3e-3, 1.6e-3, 1.2e-2]
Latissimus Dorsi, Caudal	Spine*	[1.8e-2, -3e-3, 1e-2]	Humerus	[5.5e-3, 1.7e-3, 1.1e-2]
Latissimus Dorsi, Rostral	Spine*	[1.5e-2, -7.1e-4, 1.3e-2]	Humerus	[5.9e-3, 1.5e-3, 1.1e-2]
Pectoralis Major, Anterior	Rib-cage*	[9.1e-3, -1.6e-3, 1.7e-2]	Humerus	[5.3e-3, 1.4e-3, 1.2e-2]
Pectoralis Major, Posterior	Rib-cage*	[1e-2, -3.1e-3, 1.5e-2]	Humerus	[5.5e-3, 1e-3, 1.2e-2]
Pectoralis Minor, Clavicular	Clavicle	[1.1e-2, -9.6e-4, 1.3e-2]	Humerus	[5.6e-3, 1.2e-3, 1.2e-2]
Pronator Teres	Humerus	[3.6e-3, -6.7e-4, 9.3e-3]	Radius	[8.8e-4, 1.2e-3, 1e-2]
Subscapularis	Scapula	[1.3e-2, 4e-4, 1.3e-2]	Humerus	[8.2e-3, 6.2e-4, 1.2e-2]
Triceps, Long Head	Scapula	[9.8e-3, 1.2e-3, 1.2e-2]	Ulna	[4.2e-3, -5.7e-4, 8e-3]
Triceps, Lateral Head	Humerus	[8.4e-3, 1.6e-3, 1.2e-2]	Ulna	[4.1-3, -4.5e-4, 8.3e-3]
Triceps, Medial Head	Humerus	[6.5e-3, 2.5e-4, 1.1e-2]	Ulna	[3.8e-3, -2.3e-4, 8.4e-3]

* Spinal and rib attachments made to Scapula fixed ground object.

Table 2. Muscle Parameters

Muscle Name	Max Isometric Force (N)	Optimal Fiber Length (m)	Pennation Angle (rad)	Tendon Slack Length (m)
Anconeus	0.023	0.003	0.1	0.0002
Anconeus, Short Head	0.02	0.0015	0.1	0.00015
Biceps, Long Head	0.093	0.0085	0.1	0.0002
Biceps, Short Head	0.018	0.005	0.1	0.0005
Brachialis, Proximal Head	0.066	0.007	0.1	0.0001
Brachialis, Distal Head	0.067	0.007	0.1	0.0001
Brachioradialis	0.02	0.007	0.1	0.0001
Deltoid, Medial	0.069	0.006	0.2	0.0002
Deltoid, Posterior	0.068	0.0035	0.2	0.0001
Flexorcarpiradialis	0.02	0.007	0.1	0.0001
Infraspinatus	0.065	0.003	0.2	0.0001
Latissimus Dorsi, Caudal	0.133	0.011	0.36	0.0005
Latissimus Dorsi, Rostral	0.1133	0.011	0.36	0.0005
Pectoralis Major, Anterior	0.233	0.008	0.3	0.0002
Pectoralis Major, Posterior	0.170	0.007	0.3	0.0005
Pectoralis Minor, Clavicular	0.033	0.0056	0.25	0.0002
Pronator Teres	0.02	0.003	0.1	0.0001
Subscapularis	0.34	0.005	0.2	0.0001
Triceps, Long Head	0.612	0.008	0.3	0.0007
Triceps, Lateral Head	0.125	0.007	0.17	0.0001
Triceps, Medial Head	0.16	0.004	0.2	0.0001

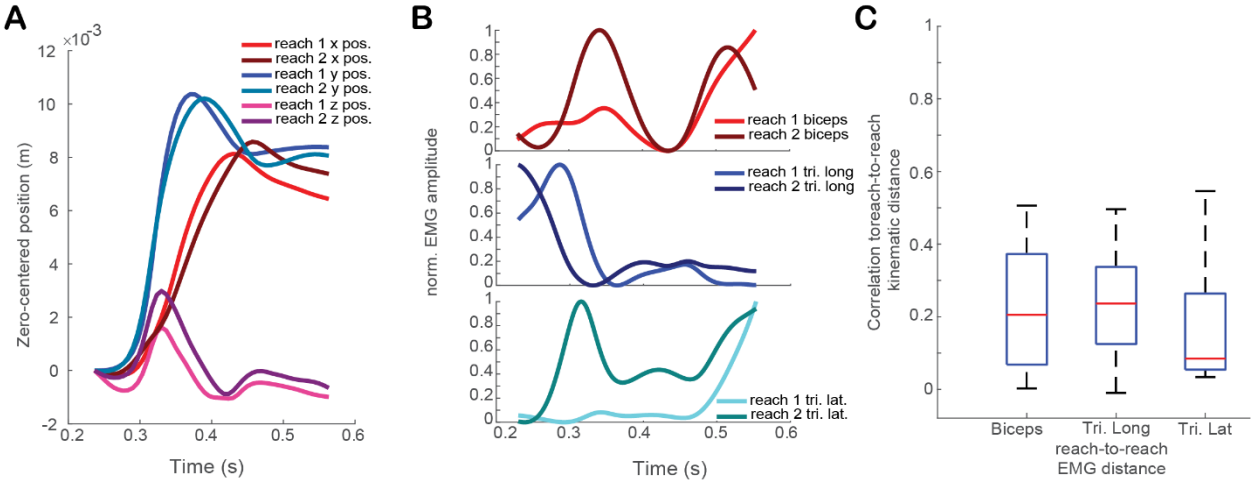

Supplemental Figure 1. Variability in electromyography between similar reaches. A. Example of two reaches that have similar trajectories, with x from teaches one and two shown in red, y in blue, and z in magenta. Reaches have been aligned to their initial position. **B.** Corresponding EMG signals from the reaches selected in A, with biceps activity for reaches one and two shown on the top panel in red, triceps long head in blue in the second panel, and triceps lateral head shown in teal in the third panel. **C.** Correlation between the Euclidean distance between reach trajectories to the distance between normalized EMG traces, showing a low to moderate effect on EMG similarity for alike reaches.